Vortex fiber nulling for exoplanet observations. I. Experimental demonstration in monochromatic light

DANIEL ECHEVERRI[1,*], GARRETH RUANE[1,†], NEMANJA JOVANOVIC[1], DIMITRI MAWET[1,2], AND NICOLAS LEVRAUD[1]

[1] Department of Astronomy, California Institute of Technology, 1200 E California Blvd, Pasadena, CA 91125, USA
[2] Jet Propulsion Laboratory, California Institute of Technology, 4800 Oak Grove Dr, Pasadena, CA 91109, USA
[*] Corresponding author: dechever@caltech.edu
[†] NSF Astronomy and Astrophysics Postdoctoral Fellow

Compiled November 7, 2018

Vortex fiber nulling (VFN) is a method for spectroscopically characterizing exoplanets at small angular separations, $\lesssim \lambda/D$, from their host star. The starlight is suppressed by creating an optical vortex in the system point spread function, which prevents the stellar field (on-axis) from coupling into the fundamental mode of a single-mode optical fiber. Light from the planet, on the other hand (slightly off-axis), couples into the fiber and is routed to a spectrograph. Using a prototype VFN designed for monochromatic light, we demonstrate coupling fractions of 6×10^{-5} and > 0.1 for the star and planet, respectively.

OCIS codes: (350.1260) Astronomical optics; (300.0300) Spectroscopy; (050.4865) Optical vortices; (060.2430) Fibers, single-mode.

http://dx.doi.org/10.1364/ao.XX.XXXXXX

1. INTRODUCTION

Detecting spectral signs of life in the atmospheres of exoplanets is a premier goal of modern astronomy. While future large-aperture space telescopes with coronagraphs may enable the direct imaging and spectroscopy of Earth-like exoplanets orbiting stars similar to our sun (see e.g. Ref. [1]), the next-generation of ground-based telescopes with adaptive optics will focus on planets in the habitable zone of cooler M dwarf stars, such as the known planets Proxima Centauri b [2] and Ross 128 b [3]. The number of planets expected to be detected and spectroscopically characterized with both space-based and ground-based facilities is, however, limited by their respective inner working angles, or the minimum angular separation from the host star where light from exoplanets may be detected. Improving sensitivity at smaller angular separations provides access to many more potential targets whose planet-to-star flux ratios are favorable due to their close proximity to their host star and increases the maximum wavelength at which they can be observed.

We present an experimental demonstration of an optical system known as a vortex fiber nuller (VFN) [4] that allows for the spectral characterization of exoplanets at angular separations less than the Rayleigh criterion; i.e. $< 1.22\,\lambda/D$, where λ is the wavelength and D is the telescope diameter. Figure 1a illustrates a VFN with a vortex phase mask [5] placed in a pupil plane to impart a phase pattern of the form $\exp(\pm i\theta)$ on the starlight (as in Ref. [6]), preventing it from coupling into a single-mode fiber (SMF) located on the optical axis in the final focal plane. Assuming the star is also aligned to the optical axis, the stellar point spread function (PSF) is rejected by the SMF because its complex field is orthogonal to the fiber's fundamental mode. For an arbitrary point source, the fraction of light that couples into the fiber as a function of its angular separation from the optical axis, α, is

$$\eta(\alpha) = \frac{\left|\int \Psi(r) f(r,\alpha) dA\right|^2}{\left|\int \Psi(r) dA\right|^2 \left|\int f(r,\alpha) dA\right|^2}, \quad (1)$$

where $\Psi(r)$ is the fiber mode and $f(r,\alpha)$ is the field in the final image plane [7]. dA is the differential area element and (r,θ) are polar coordinates in the (x,y) plane. For common SMFs, the fundamental mode can be approximated as a Gaussian with the functional form $\Psi(r) = \exp[-(2r/D_f)^2]$, where D_f is the mode field diameter. Any stellar field of the form $f(r,0) = f_r(r)\exp(\pm i\theta)$ leads to $\eta(0) = \eta_{\text{star}} = 0$. However, light from a point source (e.g. a planet) at an angular separation α will couple into the single mode fiber with the efficiency shown in Fig. 1b. The maximum theoretical coupling efficiency in this arrangement, $\eta = 19\%$, is achieved at $\alpha = 0.86\,\lambda/D$ with $D_f = 1.4\,\lambda F\#$, where $F\#$ is the focal ratio of the lens. In practice, the single mode fiber is routed to a spectrograph to measure and analyze spectral signatures in the light from the planet [8].

The VFN approach is akin to traditional nulling interferometry [9, 10], but makes use of the full telescope aperture. The key advantages are (1) the extremely small inner working angle, (2) the rotational symmetry of the coupling function which allows for spectral follow up of planets when the azimuthal orientation of their orbits are uncertain, and (3) the theoretically wavelength-independent nulling of starlight. Here, we demonstrate the predicted nulling effect in the laboratory using a prototype system designed for monochromatic light.

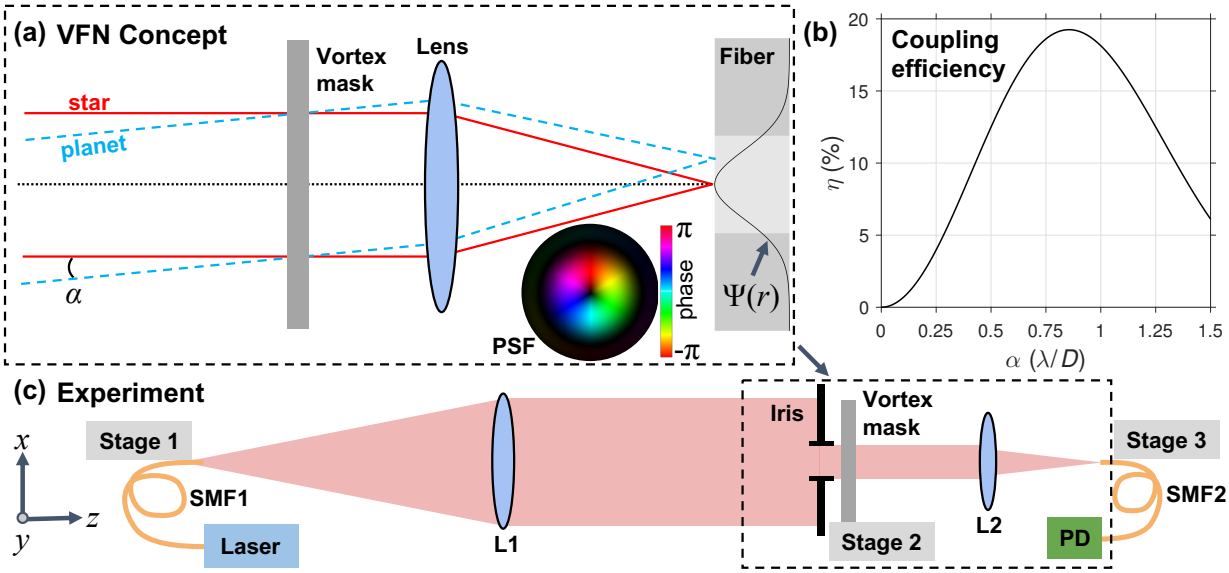

Fig. 1. (a) Schematic of a vortex fiber nuller (VFN). Light from the star (red rays) and planet (blue rays) passes through a vortex mask with complex transmittance $\exp(\pm i\theta)$. The image of the star is aligned to a single mode fiber on the optical axis with fundamental mode, $\Psi(r)$, whereas the planet image is slightly off-axis. Each has a point spread function (PSF) characterized by a donut shape in intensity and phase proportional to the azimuthal angle. (b) Coupling efficiency, η, for a point source at angular separation, α. (c) Diagram of the prototype VFN demonstrated here. Light from a fiber-coupled laser source launched by SMF1 is collimated by lens L1 (focal length $f = 200$ mm) and evenly illuminates a circular iris, which defines the pupil. The beam passes through a liquid crystal vector vortex mask directly behind the iris and is then focused by lens L2 ($f = 11$ mm) onto SMF2. We measure the coupled power using photodiode PD. Stages 1 and 3 are five-axis stages while stage 2 is a two-axis stage. Linear actuators allow computer-controlled motion in the x and y directions for the vortex mask and x, y, and z for SMF2.

2. EXPERIMENTAL SETUP

Figure 1c shows a diagram of the experimental optical layout. Light from a SMF-coupled laser diode operating at $\lambda = 635$ nm (Thorlabs KLS635) is collimated by a 200 mm focal length lens (L1; Thorlabs AC254-200-A) and evenly illuminates a 3.6 mm diameter iris. A liquid crystal vector vortex mask (Thorlabs WPV-10L-633), placed immediately after the iris, applies the desired phase pattern to the incoming beam in the pupil plane. Computer-controlled linear actuators (Zaber X-NA08A25) on stage 2 provide fine transverse alignment (25 mm travel, < 1 μm repeatability) of the vortex mask in the x and y directions.

The vortex mask is a half wave plate with a spatially-variant fast axis angle, $\chi = \theta/2$. The transmitted complex field is $E_{R,L} = \exp(\pm i2\chi)E_{L,R}$, where E_R and E_L are the right and left circularly polarized components, respectively [11]. The two output components have conjugate vortex phases of the form $\exp(\pm i\theta)$ and a polarization state that is orthogonal to the input. The mask is optimized to provide the half wave retardance, and thus the vortex phase, at a single wavelength, $\lambda = 633$ nm.

An 11-mm focal length aspheric lens (L2; Thorlabs A-397TM-A) focuses the beam on to the detection fiber (SMF2), which is centered on the optical axis and connected to a variable gain silicon photodiode (PD; Femto OE-200-SI). The source and detector SMFs, respectively SMF1 and SMF2, are SM600 fibers with D_f =3.6-5.3 μm and a single mode cutoff wavelength of 500-600 nm. Each is fixed to a manual 5-axis stage (stages 1 and 3; degrees of freedom: x, y, z, tip, and tilt). Three computer-controlled piezo actuators (Thorlabs PE4) attached to stage 3 position SMF2 to an accuracy of 10 nm (15 μm travel) in the x, y, and z directions.

During alignment, we used a Shack-Hartmann wavefront sensor (ImagineOptic, HASO4-Broadband) to measure and help minimize the static aberration in the final focal plane. The total wavefront error through the two lenses and vortex mask substrate was 7.3 nm RMS ($\sim \lambda/100$). The wavefront sensor also provided the amplitude of each of the lowest 32 Zernike modes, which will be exploited in a later section.

To determine the maximum coupling efficiency, we offset the vortex mask in the x direction such that the beam passed through a region far from the phase singularity and then co-aligned SMF1 and SMF2. In this configuration, the coupling efficiency was 56% rather than the theoretical maximum of 82%. We attribute 0.4% of the coupling loss to the measured wavefront error and the remainder to a mismatch between the focal ratio of the system (F#=3.1) and that which would provide maximum coupling into SMF2 (F#=4.1-6.0). Indeed, for a F#=3.1 beam, the optimum theoretical coupling efficiency is 57%, which is in good agreement with the measured value.

3. PROCEDURE

The objective of the experimental procedure was (1) to demonstrate that light from an unresolved source on the optical axis is prevented from coupling into SMF2 and (2) to show that light from an off-axis source couples into SMF2 with the predicted efficiency. Given the symmetry in our setup, translating SMF1 or SMF2 in the (x, y) plane is equivalent, barring a magnification factor. Therefore, for experimental convenience, we opted to measure the coupling efficiency as a function of the position of SMF2 using highly-accurate piezo actuators.

In order to ensure that aberrations were minimized, we removed stage 3 and SMF2 and used an additional lens and CMOS detector (Thorlabs DCC1545M) to take images of the PSF with

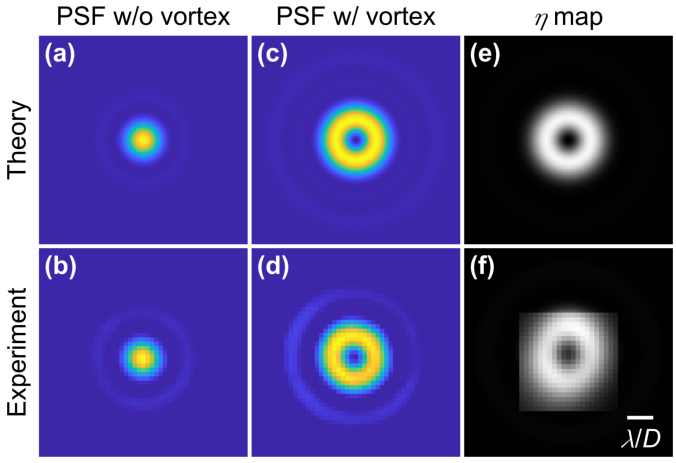

Fig. 2. PSFs (a)-(b) without and (c)-(d) with the vortex mask centered on the pupil. (e)-(f) Coupling efficiency as a function of the angular separation of SMF2, or equivalently the source, from the optical axis (0.35 μm step size). The theoretical predictions match well with our experimental results. The PSF images and coupling map have six samples per $\lambda F\#$.

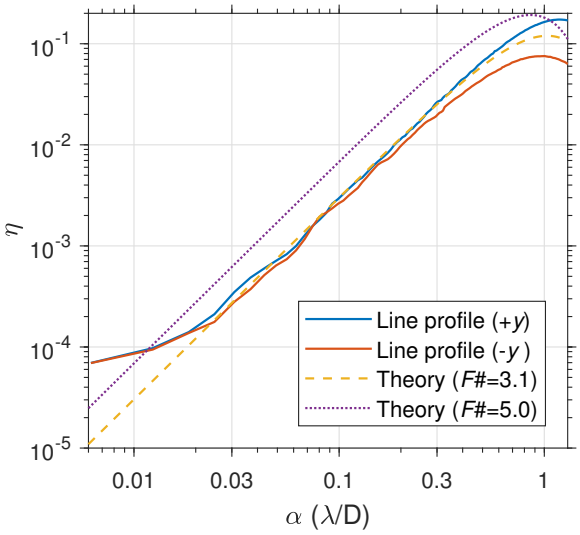

Fig. 3. Linear scans of SMF2 in the $\pm y$ directions with a 12 nm step size. The best achieved null $\eta_{\text{star}} = \eta(0) = 6 \times 10^{-5}$, which is likely limited by static aberrations. Our measurements match well with the theoretical line profiles for our system ($F\# = 3.1$). However, $F\# = 5.0$ is required to achieve the ideal performance.

and without the vortex mask. Then, with stage 3 and SMF2 back in place, we performed several two-dimensional raster scans of SMF2 in a 7×7 μm square adjusting the position of the vortex mask between each scan until we minimized the coupling for the simulated star, η_{star}.

At each SMF2 position, we checked that the power measured by the PD was above the predetermined noise floor and then averaged 100 measurements before moving SMF2 to the next location. Once each full 2D scan was completed, we inserted a calibrated power meter (Thorlabs PM100D, S120C) in front of SMF2 and measured the total power in the beam to normalize the signal at the output. Finally, we determined the bias signal of the PD by blocking the light source and subtracted the bias from our measurements. To obtain η, we normalized the measured power by the total power accounting for the transmission of SMF2, including the Fresnel reflections at both ends (3.46% per facet) as well as propagation losses (0.34% per meter).

4. RESULTS

Figure 2 shows images of the PSF at the plane of SMF2 (Figure 2a-d) and the two-dimensional coupling maps obtained by scanning SMF2 in the (x, y) plane. The PSF images with the beam passing through the edge of the vortex mask (Fig. 2b) resembles an Airy pattern (Fig. 2a) validating that the collimated beam evenly illuminates the iris. The PSF with the vortex centered on the iris (Fig. 2d) appears annular in shape as predicted (Fig. 2c). The ideal coupling efficiency as a function of the 2D position of SMF2 (see Fig. 2e) is a donut shape with the radial profile in Fig. 1b. The measured coupling map (Fig. 2f) shows a very similar shape except for a slight vertical elongation likely owing to imperfect calibration of the piezo actuator gains.

In addition to the 2D coupling map in Fig. 2f, we took two fine linear scans starting at the deepest null found and moving radially outward in the $\pm y$ directions in 12 nm steps (see Fig. 3). The deepest null measured, with SMF1 and SMF2 on the optical axis, was $\eta_{\text{star}} = 6 \times 10^{-5}$. The maximum coupling efficiency for the line scans was $\eta = 8\%$ and 15% for the $\pm y$ directions, respectively, revealing an asymmetry in the coupling map. We compare our line scan measurements with the theoretical line profiles for an ideal system ($F\#$=5.0) and our setup ($F\#$=3.1). The laboratory-measured line profiles are in close agreement with our theoretical predication showing a minor departure at $\alpha \lesssim 0.02\ \lambda/D$ and $\alpha \gtrsim 0.3\ \lambda/D$. We expect that optimizing the focal ratio would improve the theoretical maximum coupling efficiency from 12% up to a maximum of 19% and the peak would shift from $\alpha = \lambda/D$ to $\alpha = 0.86\ \lambda/D$.

5. DISCUSSION

Although the experimental PSFs (Fig. 2b,d) are in close agreement with theory (Fig. 2a,c), the diffraction rings are slightly more pronounced than expected. This is likely due to spherical aberration unseen by our wavefront sensor, which we used in a diverging beam after L2's focus and therefore discarded all power terms.

Using our wavefront error measurements, we estimate the minimum possible η_{star} by numerically computing Eqn. 1. Following Ref. [4], we determined the sensitivity of the null to low-order Zernike aberrations, Z_n^m. For each Zernike mode, we fit the response function $\eta_{\text{star}} = (b\omega)^2$, where b is the sensitivity coefficient and ω is the RMS wavefront error in units of waves. By orthogonality, the sensitivity coefficient is zero for all Zernike modes Z_n^m where $m \neq \pm 1$. Also, the precision of the piezo actuators mitigates the tip and tilt errors. Thus, our experimental nulls are likely limited by coma aberrations. Table 1 lists the measured wavefront error in the $m \neq \pm 1$ coma modes as well as their corresponding b value and predicted contribution to η_{star}. Taking the linear combination of the individual error contributions predicts a minimum null of $\eta_{\text{star}} = 5.0 \times 10^{-5}$, which is in good agreement with the minimum null measured in the line scans, $\eta_{\text{star}} = 6.0 \times 10^{-5}$.

The line scans presented in Fig. 3 reveal an asymmetry in peak coupling efficiency around the donut. In that case, to achieve the smallest value of η_{star}, we scanned both the position of the vortex

Table 1. Measured wavefront error, ω, in the coma Zernike modes, $Z_n^{\pm 1}$, and expected stellar leakage, $\eta_{\rm star} = (b\omega)^2$, for (0°,90°) aberrations, where b is the aberration sensitivity coefficient. All other modes have $b = 0$.

Modes	ω (waves RMS)	b	η_s
$Z_3^{\pm 1}$	(-1.7,-2.8)$\times 10^{-3}$	2.15	(1.3,3.6)$\times 10^{-5}$
$Z_5^{\pm 1}$	(0.1,-0.2)$\times 10^{-3}$	1.12	(1.3,5.0)$\times 10^{-8}$
$Z_7^{\pm 1}$	(-0.7,0.0)$\times 10^{-3}$	0.67	(2.2,0.0)$\times 10^{-7}$
Total			5.0×10^{-5}

mask in addition to SMF2. Using numerical simulations, we find that, in the presence of coma aberrations, the optimal null occurs when the vortex mask is slightly off-center causing the coupling map to become asymmetric. This implies that, when observing an exoplanet with a known orbit around its host star, it may be possible to deliberately misalign the vortex in the pupil to create an asymmetric coupling map which preferentially couples more light at the location of the planet. Maximizing the throughput for the planet is important as the integration time scales as the inverse square of planet's coupling efficiency, η^{-2}, in the stellar photon noise limited regime [4].

The shape of the pupil has little influence on the performance of the VFN [4]; the results presented here are also valid for non-circular, obstructed, and segmented apertures. In fact, the pupil created by the iris used in these experiments was only quasi-circular in shape, with 10-12 flat edges. Future experiments will make use of a pupil mask that mimics the boundaries of an actual telescope pupil.

We have demonstrated that the VFN concept in monochromatic light with a simple and inexpensive optical system. However, exoplanet spectroscopy requires similar starlight suppression levels in polychromatic light. We plan to build a polychromatic testbed using off-axis parabolic mirrors instead of transmissive lenses, a carefully matched $F\#$, and broadband vortex masks optimized for the optical and infrared regimes. Vortex masks that apply the same phase pattern as a function of wavelength have been demonstrated using polarization dependent, or "vector," methods: liquid crystals [12], sub-wavelength gratings [13], and photonic crystal structures [14]. Achromatic scalar masks are also possible [15].

Furthermore, we plan to integrate a polychromatic VFN into an adaptive optics system with a deformable mirror, similar to previous fiber injection instruments tested by our team [16], which will allow us to develop wavefront sensing and control techniques to maintain the null in the presence of realistic wavefront errors and flux levels. Ultimately, our goal is to integrate a VFN module into the Keck Planet Imager and Characterizer at the W.M. Keck Observatory [17] to open up the possibility of characterizing the reflected light spectrum of giant exoplanets whose properties have so far only been inferred based on stellar radial velocity measurements. This will pave the way to characterizing smaller, potentially habitable planets with future large-aperture telescopes.

6. CONCLUSIONS

We have demonstrated the VFN concept in a laboratory for the first time. Using a prototype system designed for monochromatic light, we have demonstrated a stellar coupling fraction of $\eta_{\rm star} = 6.0 \times 10^{-5}$ and peak planet coupling efficiencies of η=8-15% at an angular separation of $\alpha \approx \lambda/D$. Discrepancies between our measurements and the predicted performance are attributed to a mismatch between our experimental $F\#$ and that which is optimal for a VFN system. We predict that using the ideal $F\#$ and minimizing wavefront error will yield $\eta = 19\%$ at 0.86 λ/D in all azimuthal directions. We have identified a clear pathway to achieving similar performance in polychromatic light and to develop the wavefront sensing and control techniques needed for on-sky operation.

The VFN concept is a promising approach for reducing the stellar photon noise that otherwise inhibits the characterization of exoplanets whose angular separations are within the inner working angle of conventional coronagraphs. We expect that this technique will open the possibility to measure the reflected light spectrum of exoplanets inferred from stellar radial velocity measurements and thereby allow for the detailed characterization of their atmospheres for the first time. Such planets are often at angular separations of $\alpha \lesssim \lambda/D$, which is currently too close to the star to characterize by other means. We envisage that VFN will significantly increase the number of exoplanets, from rocky worlds to gas giants, characterized by current and future ground- and space-based telescopes.

Funding. G. Ruane is supported by the National Science Foundation (NSF) (AST-1602444). Part of this work was supported by RTD program at the Jet Propulsion Laboratory, California Institute of Technology, under contract with the National Aeronautics and Space Administration (NASA).

REFERENCES

1. G. Ruane, D. Mawet, B. Mennesson, J. Jewell, and S. Shaklan, J. Astron. Telesc. Instrum. Syst. **4**, 015004 (2018).
2. G. Anglada-Escudé, P. J. Amado, J. Barnes, Z. M. Berdiñas, R. P. Butler, G. A. L. Coleman, I. de la Cueva, S. Dreizler, M. Endl, B. Giesers, S. V. Jeffers, J. S. Jenkins, H. R. A. Jones, M. Kiraga, M. Kürster, M. J. López-González, C. J. Marvin, N. Morales, J. Morin, R. P. Nelson, J. Ortiz, A. Ofir, S.-J. Paardekooper, A. Reiners, E. Rodríguez, C. Rodriguez-López, L. F. Sarmiento, J. P. Strachan, Y. Tsapras, M. Tuomi, and M. Zechmeister, Nature. **536**, 437 (2016).
3. X. Bonfils, N. Astudillo-Defru, R. Díaz, J.-M. Almenara, T. Forveille, F. Bouchy, X. Delfosse, C. Lovis, M. Mayor, F. Murgas, F. Pepe, N. C. Santos, D. Ségransan, S. Udry, and A. Wünsche, Astron. Astrophys. **613**, A25 (2017).
4. G. Ruane, J. Wang, D. Mawet, N. Jovanovic, J.-R. Delorme, B. Mennesson, and J. K. Wallace, Astrophys. J. (2018).
5. M. W. Beijersbergen, R. P. C. Coerwinkel, M. Kristensen, and J. P. Woerdman, Opt. Commun. **112**, 321 (1994).
6. G. A. Swartzlander, Opt. Lett. **26**, 497 (2001).
7. S. Shaklan and F. Roddier, Appl. Opt. **27**, 2334 (1988).
8. J. Wang, D. Mawet, G. Ruane, R. Hu, and B. Benneke, Astron. J. **153**, 183 (2017).
9. R. N. Bracewell, Nature. **274**, 780 (1978).
10. P. Haguenauer and E. Serabyn, Appl. Opt. **45**, 2749 (2006).
11. L. Marrucci, C. Manzo, and D. Paparo, Phys. Rev. Lett. **96**, 163905 (2006).
12. D. Mawet, E. Serabyn, K. Liewer, C. Hanot, S. McEldowney, D. Shemo, and N. O'Brien, Opt. Express **17**, 1902 (2009).
13. D. Mawet, P. Riaud, J. Surdej, and J. Baudrand, Appl. Opt. **44**, 7313 (2005).
14. N. Murakami, S. Hamaguchi, M. Sakamoto, R. Fukumoto, A. Ise, K. Oka, N. Baba, and M. Tamura, Opt. Express **21**, 7400 (2013).
15. G. A. Swartzlander, Opt. Lett. **31**, 2042 (2006).
16. D. Mawet, G. Ruane, W. Xuan, D. Echeverri, N. Klimovich, M. Randolph, J. Fucik, J. K. Wallace, J. Wang, G. Vasisht, R. Dekany, B. Mennesson,

E. Choquet, J.-R. Delorme, and E. Serabyn, Astrophys. J. **838**, 92 (2017).
17. D. Mawet, J. R. Delorme, N. Jovanovic, J. K. Wallace, R. D. Bartos, P. L. Wizinowich, M. Fitzgerald, S. Lilley, G. Ruane, J. Wang, N. Klimovich, and Y. Xin, Proc. SPIE **10400**, 1040029 (2017).

FULL REFERENCES

1. G. Ruane, D. Mawet, B. Mennesson, J. Jewell, and S. Shaklan, "Vortex coronagraphs for the Habitable Exoplanet Imaging Mission (HabEx) concept: theoretical performance and telescope requirements," J. Astron. Telesc. Instrum. Syst. **4**, 015004 (2018).
2. G. Anglada-Escudé, P. J. Amado, J. Barnes, Z. M. Berdiñas, R. P. Butler, G. A. L. Coleman, I. de la Cueva, S. Dreizler, M. Endl, B. Giesers, S. V. Jeffers, J. S. Jenkins, H. R. A. Jones, M. Kiraga, M. Kürster, M. J. López-González, C. J. Marvin, N. Morales, J. Morin, R. P. Nelson, J. Ortiz, A. Ofir, S.-J. Paardekooper, A. Reiners, E. Rodríguez, C. Rodriguez-López, L. F. Sarmiento, J. P. Strachan, Y. Tsapras, M. Tuomi, and M. Zechmeister, "A terrestrial planet candidate in a temperate orbit around Proxima Centauri," Nature. **536**, 437–440 (2016).
3. X. Bonfils, N. Astudillo-Defru, R. Díaz, J.-M. Almenara, T. Forveille, F. Bouchy, X. Delfosse, C. Lovis, M. Mayor, F. Murgas, F. Pepe, N. C. Santos, D. Ségransan, S. Udry, and A. Wünsche, "A temperate exo-Earth around a quiet M dwarf at 3.4 parsecs," Astron. Astrophys. **613**, A25 (2017).
4. G. Ruane, J. Wang, D. Mawet, N. Jovanovic, J.-R. Delorme, B. Mennesson, and J. K. Wallace, "Efficient spectroscopy of exoplanets at small angular separations with vortex fiber nulling," Astrophys. J. (2018).
5. M. W. Beijersbergen, R. P. C. Coerwinkel, M. Kristensen, and J. P. Woerdman, "Helical-wavefront laser beams produced with a spiral phaseplate," Opt. Commun. **112**, 321–327 (1994).
6. G. A. Swartzlander, "Peering into darkness with a vortex spatial filter," Opt. Lett. **26**, 497–499 (2001).
7. S. Shaklan and F. Roddier, "Coupling starlight into single-mode fiber optics," Appl. Opt. **27**, 2334–2338 (1988).
8. J. Wang, D. Mawet, G. Ruane, R. Hu, and B. Benneke, "Observing Exoplanets with High Dispersion Coronagraphy. I. The Scientific Potential of Current and Next-generation Large Ground and Space Telescopes," Astron. J. **153**, 183 (2017).
9. R. N. Bracewell, "Detecting nonsolar planets by spinning infrared interferometer," Nature. **274**, 780 (1978).
10. P. Haguenauer and E. Serabyn, "Deep nulling of laser light with a single-mode-fiber beam combiner," Appl. Opt. **45**, 2749–2754 (2006).
11. L. Marrucci, C. Manzo, and D. Paparo, "Optical spin-to-orbital angular momentum conversion in inhomogeneous anisotropic media," Phys. Rev. Lett. **96**, 163905 (2006).
12. D. Mawet, E. Serabyn, K. Liewer, C. Hanot, S. McEldowney, D. Shemo, and N. O'Brien, "Optical vectorial vortex coronagraphs using liquid crystal polymers: theory, manufacturing and laboratory demonstration," Opt. Express **17**, 1902–1918 (2009).
13. D. Mawet, P. Riaud, J. Surdej, and J. Baudrand, "Subwavelength surface-relief gratings for stellar coronagraphy," Appl. Opt. **44**, 7313–7321 (2005).
14. N. Murakami, S. Hamaguchi, M. Sakamoto, R. Fukumoto, A. Ise, K. Oka, N. Baba, and M. Tamura, "Design and laboratory demonstration of an achromatic vector vortex coronagraph," Opt. Express **21**, 7400 (2013).
15. G. A. Swartzlander, "Achromatic optical vortex lens," Opt. Lett. **31**, 2042–2044 (2006).
16. D. Mawet, G. Ruane, W. Xuan, D. Echeverri, N. Klimovich, M. Randolph, J. Fucik, J. K. Wallace, J. Wang, G. Vasisht, R. Dekany, B. Mennesson, E. Choquet, J.-R. Delorme, and E. Serabyn, "Observing Exoplanets with High-dispersion Coronagraphy. II. Demonstration of an Active Single-mode Fiber Injection Unit," Astrophys. J. **838**, 92 (2017).
17. D. Mawet, J. R. Delorme, N. Jovanovic, J. K. Wallace, R. D. Bartos, P. L. Wizinowich, M. Fitzgerald, S. Lilley, G. Ruane, J. Wang, N. Klimovich, and Y. Xin, "A fiber injection unit for the Keck Planet Imager and Characterizer," Proc. SPIE **10400**, 1040029 (2017).